Kinematic evidence for bipolar ejecta flows in the Galactic supernova remnant W49B

Audard, M.; Awaki, H.; Ballhausen, R.; Bamba, A.; Behar, E.; Boissay-Malaquin, R.; ... ; Suzuki, N.

Note: To cite this publication please use the final published version (if applicable).

Kinematic Evidence for Bipolar Ejecta Flows in the Galactic Supernova Remnant W49B

XRISM Collaboration, Marc Audard[1], Hisamitsu Awaki[2], Ralf Ballhausen[3,4,5], Aya Bamba[6], Ehud Behar[7], Rozenn Boissay-Malaquin[8,4,5], Laura Brenneman[9], Gregory V. Brown[10], Lia Corrales[11], Elisa Costantini[12], Renata Cumbee[4], María Díaz Trigo[13], Chris Done[14], Tadayasu Dotani[15], Ken Ebisawa[15], Megan E. Eckart[10], Dominique Eckert[1], Satoshi Eguchi[16], Teruaki Enoto[17], Yuichiro Ezoe[18], Adam Foster[9], Ryuichi Fujimoto[15], Yutaka Fujita[18], Yasushi Fukazawa[19], Kotaro Fukushima[15], Akihiro Furuzawa[20], Luigi Gallo[21], Javier A. García[4,22], Liyi Gu[12], Matteo Guainazzi[23], Kouichi Hagino[6], Kenji Hamaguchi[8,4,5], Isamu Hatsukade[24], Katsuhiro Hayashi[15], Takayuki Hayashi[8,4,5], Natalie Hell[10], Edmund Hodges-Kluck[4], Ann Hornschemeier[4], Yuto Ichinohe[25], Daiki Ishi[15], Manabu Ishida[15], Kumi Ishikawa[18], Yoshitaka Ishisaki[18], Jelle Kaastra[12,26], Timothy Kallman[4], Erin Kara[27], Satoru Katsuda[28], Yoshiaki Kanemaru[15], Richard L. Kelley[4], Caroline A. Kilbourne[4], Shunji Kitamoto[29], Shogo Kobayashi[30], Takayoshi Kohmura[31], Aya Kubota[32], Maurice A. Leutenegger[4], Michael Loewenstein[3,4,5], Yoshitomo Maeda[15], Maxim Markevitch[4], Hironori Matsumoto[33], Kyoko Matsushita[30], Dan McCammon[34], Brian McNamara[35], François Mernier[3,4,5], Eric D. Miller[27], Jon M. Miller[11], Ikuyuki Mitsuishi[36], Misaki Mizumoto[37], Tsunefumi Mizuno[38], Koji Mori[24], Koji Mukai[8,4,5], Hiroshi Murakami[39], Richard Mushotzky[3], Hiroshi Nakajima[40], Kazuhiro Nakazawa[36], Jan-Uwe Ness[41], Kumiko Nobukawa[42], Masayoshi Nobukawa[43], Hirofumi Noda[44], Hirokazu Odaka[33], Shoji Ogawa[15], Anna Ogorzalek[3,4,5], Takashi Okajima[4], Naomi Ota[45], Stephane Paltani[1], Robert Petre[4], Paul Plucinsky[9], Frederick S. Porter[4], Katja Pottschmidt[8,4,5], Hidetoshi Sano[46], Kosuke Sato[47], Toshiki Sato[48], Makoto Sawada[29,49], Hiromi Seta[18], Megumi Shidatsu[2], Aurora Simionescu[12], Randall Smith[9], Hiromasa Suzuki[15], Andrew Szymkowiak[50], Hiromitsu Takahashi[19], Mai Takeo[51], Toru Tamagawa[25], Keisuke Tamura[8,4,5], Takaaki Tanaka[52], Atsushi Tanimoto[53], Makoto Tashiro[28,15], Yukikatsu Terada[28,15], Yuichi Terashima[2], Yohko Tsuboi[54], Masahiro Tsujimoto[15], Hiroshi Tsunemi[33], Takeshi G. Tsuru[17], Ayşegül Tümer[4,5,8], Hiroyuki Uchida[17], Nagomi Uchida[15], Yuusuke Uchida[31], Hideki Uchiyama[55], Yoshihiro Ueda[56], Shinichiro Uno[57], Jacco Vink[58,12], Shin Watanabe[15], Brian J. Williams[4], Satoshi Yamada[49], Shinya Yamada[29], Hiroya Yamaguchi[15], Kazutaka Yamaoka[36], Noriko Yamasaki[15], Makoto Yamauchi[24], Shigeo Yamauchi[45], Tahir Yaqoob[8,4,5], Tomokage Yoneyama[54], Tessei Yoshida[15], Mihoko Yukita[59,4], Irina Zhuravleva[60], Yuki Amano[15], Amy Gall[9], Sharon Mitrani[7], Kaito Murakami[33], Roi Rahin[4], and Nari Suzuki[45]

[1] Department of Astronomy, University of Geneva, Versoix CH-1290, Switzerland
[2] Department of Physics, Ehime University, Ehime 790-8577, Japan
[3] Department of Astronomy, University of Maryland, College Park, MD 20742, USA
[4] NASA/Goddard Space Flight Center, Greenbelt, MD 20771, USA
[5] Center for Research and Exploration in Space Science and Technology, NASA/GSFC (CRESST II), Greenbelt, MD 20771, USA
[6] Department of Physics, University of Tokyo, Tokyo 113-0033, Japan
[7] Department of Physics, Technion, Haifa 3200003, Israel
[8] Center for Space Sciences and Technology, University of Maryland, Baltimore County (UMBC), Baltimore, MD 21250, USA
[9] Center for Astrophysics—Harvard-Smithsonian, Cambridge, MA 02138, USA
[10] Lawrence Livermore National Laboratory, Livermore, CA 94550, USA
[11] Department of Astronomy, University of Michigan, Ann Arbor, MI 48109, USA
[12] SRON Netherlands Institute for Space Research, 2333 CA Leiden, The Netherlands
[13] ESO, 85748 Garching bei München, Germany
[14] Centre for Extragalactic Astronomy, Department of Physics, University of Durham, Durham DH1 3LE, UK
[15] Institute of Space and Astronautical Science (ISAS), Japan Aerospace Exploration Agency (JAXA), Kanagawa 252-5210, Japan
[16] Department of Economics, Kumamoto Gakuen University, Kumamoto 862-8680, Japan
[17] Department of Physics, Kyoto University, Kyoto 606-8502, Japan
[18] Department of Physics, Tokyo Metropolitan University, Tokyo 192-0397, Japan
[19] Department of Physics, Hiroshima University, Hiroshima 739-8526, Japan
[20] Department of Physics, Fujita Health University, Aichi 470-1192, Japan
[21] Department of Astronomy and Physics, Saint Mary's University, Halifax, NS B3H 3C3, Canada
[22] California Institute of Technology, Pasadena, CA 91125, USA
[23] European Space Agency (ESA), European Space Research and Technology Centre (ESTEC), 2200 AG Noordwijk, The Netherlands
[24] Faculty of Engineering, University of Miyazaki, Miyazaki 889-2192, Japan
[25] RIKEN Nishina Center, Saitama 351-0198, Japan
[26] Leiden Observatory, University of Leiden, NL-2300 RA Leiden, The Netherlands
[27] Kavli Institute for Astrophysics and Space Research, Massachusetts Institute of Technology, Cambridge, MA 02139, USA
[28] Department of Physics, Saitama University, Saitama 338-8570, Japan
[29] Department of Physics, Rikkyo University, Tokyo 171-8501, Japan; makoto.sawada@rikkyo.ac.jp
[30] Faculty of Physics, Tokyo University of Science, Tokyo 162-8601, Japan
[31] Faculty of Science and Technology, Tokyo University of Science, Chiba 278-8510, Japan
[32] Department of Electronic Information Systems, Shibaura Institute of Technology, Saitama 337-8570, Japan
[33] Department of Earth and Space Science, Osaka University, Osaka 560-0043, Japan
[34] Department of Physics, University of Wisconsin–Madison, Madison, WI 53706, USA
[35] Department of Physics and Astronomy, Waterloo Centre for Astrophysics, University of Waterloo, Waterloo, ON N2L 3G1, Canada
[36] Department of Physics, Nagoya University, Aichi 464-8602, Japan
[37] Science Research Education Unit, University of Teacher Education Fukuoka, Fukuoka 811-4192, Japan

^{38} Hiroshima Astrophysical Science Center, Hiroshima University, Hiroshima 739-8526, Japan
^{39} Department of Data Science, Tohoku Gakuin University, Miyagi 984-8588, Japan
^{40} College of Science and Engineering, Kanto Gakuin University, Kanagawa 236-8501, Japan
^{41} European Space Agency (ESA), European Space Astronomy Centre (ESAC), E-28692 Madrid, Spain
^{42} Department of Science, Faculty of Science and Engineering, KINDAI University, Osaka 577-8502, Japan
^{43} Department of Teacher Training and School Education, Nara University of Education, Nara 630-8528, Japan
^{44} Astronomical Institute, Tohoku University, Miyagi 980-8578, Japan
^{45} Department of Physics, Nara Women's University, Nara 630-8506, Japan
^{46} Faculty of Engineering, Gifu University, Gifu 501-1193, Japan
^{47} Department of Astrophysics and Atmospheric Sciences, Kyoto Sangyo University, Kyoto 603-8555, Japan
^{48} School of Science and Technology, Meiji University, Kanagawa 214-8571, Japan
^{49} RIKEN Cluster for Pioneering Research, Saitama 351-0198, Japan
^{50} Yale Center for Astronomy and Astrophysics, Yale University, New Haven, CT 06520, USA
^{51} Department of Physics, Toyama University, Toyama 930-8555, Japan
^{52} Department of Physics, Konan University, Hyogo 658-8501, Japan
^{53} Graduate School of Science and Engineering, Kagoshima University, Kagoshima 890-8580, Japan
^{54} Department of Physics, Chuo University, Tokyo 112-8551, Japan
^{55} Faculty of Education, Shizuoka University, Shizuoka 422-8529, Japan
^{56} Department of Astronomy, Kyoto University, Kyoto 606-8502, Japan
^{57} Nihon Fukushi University, Shizuoka 422-8529, Japan
^{58} Anton Pannekoek Institute, the University of Amsterdam, Postbus 942491090 GE Amsterdam, The Netherlands
^{59} Johns Hopkins University, Baltimore, MD 21218, USA
^{60} Department of Astronomy and Astrophysics, University of Chicago, Chicago, IL 60637, USA

Abstract

W49B is a unique Galactic supernova remnant with centrally peaked, "bar"-like ejecta distribution, which was once considered evidence for a hypernova origin that resulted in a bipolar ejection of the stellar core. However, chemical abundance measurements contradict this interpretation. Closely connected to the morphology of the ejecta is its velocity distribution, which provides critical details for understanding the explosion mechanism. We report the first ever observational constraint on the kinematics of the ejecta in W49B using the Resolve microcalorimeter spectrometer on the X-ray Imaging and Spectroscopy Mission (XRISM). Using XRISM/Resolve, we measured the line-of-sight velocity traced by the Fe Heα emission, which is the brightest feature in the Resolve spectrum, to vary by $\pm 300\,\mathrm{km\,s^{-1}}$ with a smooth east-to-west gradient of a few tens of kilometers per second per parsec along the major axis. Similar trends in the line-of-sight velocity structure were found for other Fe-group elements Cr and Mn, traced by the Heα emission, and also for intermediate-mass elements Si, S, Ar, and Ca, traced by the Lyα emission. The discovery of the east–west gradient in the line-of-sight velocity, together with the absence of a twin-peaked line profile or enhanced broadening in the central region, clearly rejects the equatorially expanding disk model. In contrast, the observed velocity structure suggests bipolar flows reminiscent of a bipolar explosion scenario. An alternative scenario would be a collimation of the ejecta by an elongated cavity sculpted by bipolar stellar winds.

Unified Astronomy Thesaurus concepts: Supernova remnants (1667); X-ray astronomy (1810); High resolution spectroscopy (2096)

1. Introduction

Spatial and velocity distributions of ejecta are key diagnostics used to probe the explosion mechanism and shock physics of supernova remnants (SNRs). Reverse-shocked layers of ejecta observed in young SNRs are believed to produce shell-like structure. There are also a growing number of so-called mixed-morphology SNRs (MM SNRs; J. Rho & R. Petre 1998) in which centrally peaked X-rays fill radio-shell interiors. This peculiar structure triggered decades-long discussions, and attempts to theoretically model the morphology still continue today (R. L. White & K. S. Long 1991; R. L. Shelton 1999; T. Shimizu et al. 2012; A. Chiotellis et al. 2024). The supersolar chemical abundances measured at the central region of some of MM SNRs indicate an ejecta origin for the interior of these remnants (e.g., F. Bocchino et al. 2009). Although the velocity structure would provide insight as to the origin of the morphology, there has been no robust

imaging measurement of proper motion in MM SNRs. In addition, there has been no detection of significant Doppler shifts with X-ray CCD-based spectrometers. This may be because the ejecta speed is an order of magnitude slower, i.e., below the detection limit of the moderate energy resolution of CCDs, compared to young shell-like SNRs, where a high speed of the order of $1000\,\mathrm{km\,s^{-1}}$ is often detected (e.g., A. Hayato et al. 2010; T. Sato & J. P. Hughes 2017; B. J. Williams et al. 2018).

The Galactic SNR W49B (G. Westerhout 1958; P. G. Mezger et al. 1967; C. G. Wynn-Williams 1969) is most likely the youngest member of MM SNRs based on its small size of $\approx 4' \times 3'$ or $\sim 10\,\mathrm{pc}$ at the estimated distance of 11.3 kpc (C. L. Brogan & T. H. Troland 2001; H. Sano et al. 2021) and its high electron temperature of $\approx 1.5\,\mathrm{keV}$ (M. Ozawa et al. 2009). W49B is host to an overionized/recombining plasma (M. Ozawa et al. 2009; H. Yamaguchi et al. 2018) with one of the highest average charge states of Fe ions among all SNRs, i.e., the peak of the charge-state distribution is between Fe XXVI and Fe XXV (H. Yamaguchi et al. 2014). W49B also exhibits hard X-rays originating from nonthermal bremsstrahlung of mildly energetic electrons with

kinetic energies of the order of 10 keV (T. Tanaka et al. 2018). These features make this remnant arguably the most interesting example of MM SNRs. The distribution of the ejecta-dominated X-ray emission consists of a bar-like structure running through the center with flaring at its eastern and western ends in addition to a more circular and diffuse structure. The bar-like structure is more pronounced in Fe, while the diffuse, circular structure is pronounced in lighter elements such as Si and S (R. Fujimoto et al. 1995; J. W. Keohane et al. 2007). The longer-wavelength counterparts create a barrel shape with coaxial rings in the near-infrared [Fe II] line and ear-like partial shells located at the eastern and western ends in the molecular hydrogen line, which are also bright in the radio continuum (D. A. Moffett & S. P. Reynolds 1994; W. T. Reach et al. 2006; J. W. Keohane et al. 2007). The alignment of the bar-like Fe ejecta along the axis of the infrared coaxial rings was considered evidence for jets resulting from a bipolar explosion of a supermassive star (J. W. Keohane et al. 2007; L. A. Lopez et al. 2013). This interpretation, however, contradicts abundance measurements (e.g., U. Hwang et al. 2000; P. Zhou & J. Vink 2018; L. Sun & Y. Chen 2020; T. Sato et al. 2025; M. Sawada et al. 2025), which suggest a Type Ia explosion or a Type II explosion of a relatively low mass star. Therefore, the SN origin of this unique remnant is still unknown.

A new observatory for X-ray astrophysics, the X-ray Imaging and Spectroscopy Mission (XRISM; M. S. Tashiro 2022), successfully began observations in 2023 September. XRISM carries two instruments: the Resolve high-resolution X-ray microcalorimeter spectrometer (Y. Ishisaki et al. 2022), and the Xtend wide-band X-ray CCD imager (K. Mori et al. 2022; H. Noda et al. 2025). With the requirements of the spectral resolution of $\leqslant 7$ eV at the full width at half-maximum (FWHM) at 6 keV and the absolute energy scale accuracy of $\leqslant 2$ eV, Resolve enables us to resolve and identify many lines for the first time from a variety of highly ionized atoms in W49B, including, in many cases, fine-structure lines. These well-resolved features can now be used to probe the line-of-sight (LOS) velocity of X-ray-emitting objects such as SNR ejecta to the level of ≈ 100 km s^{-1} in the Fe K band. This is an improvement of over an order of magnitude compared to previous measurements.

In this Letter, we report the discovery of a systematic gradient in the LOS velocity along the Fe ejecta, which we claim is kinematic evidence for the bipolar flows of the ejecta. We also discuss the elemental dependence of the LOS velocity gradient and what that implies about the origin of W49B. The Letter is structured as follows: The observations and data reduction are described in Section 2. The spectral analysis and results from the Resolve spectrometer data are presented in Section 3. The implications are discussed in Section 4. Finally, the Letter is summarized in Section 5.

2. Observations and Data Reduction

To cover nearly the entire $\approx 4' \times 3'$ remnant with the field of view (FOV) of $\approx 3' \times 3'$, XRISM's Resolve observed W49B with two aim points. The first, dubbed "East" (observation ID 300055010), started on 2024 April 23, while the second, dubbed "West" (observation ID 300056010), started on 2024 April 30. Each observation lasted for about 1 week.

Data analysis proceeded from cleaned events created using the pipeline-processing version 03.00.011.008 using the standard data-screening criteria.[61] In this screening, time intervals with Earth occultations and passages of the South Atlantic Anomaly were removed for both Resolve and Xtend data. In the case of Resolve, time intervals during the recycling of the adiabatic demagnetization refrigerator, those with the use of the onboard ^{55}Fe calibration sources on the instrument filter wheel (FW) for the gain monitoring, and events for diagnostic purposes (e.g., baseline events and event-lost pseudoevents) were also removed. In addition, non-X-ray events produced when cosmic rays interact with the Si frame around the detector pixels (frame events: C. A. Kilbourne et al. 2018) were identified and removed with their anomalously shaped detector pulses by using the event parameters `RISE_TIME` and `DERIV_MAX` according to Y. Mochizuki et al. (2024). The exact criteria on these parameters are described as the Resolve rise-time screening in the XRISM quick start guide v2.3.[62]

The pointing stability of the spacecraft during both observations was checked using the enhanced housekeeping file included as part of the auxiliary files of the XRISM data products. A periodic excursion of the aim point associated with the orbital period of the spacecraft was discovered. In more than 90% of the exposure times, the aim point exhibited an offset smaller than a few arcseconds, while a $\approx 30''$ offset was found in the remaining time. For each observation, the time intervals with the larger pointing offset were removed. The net exposure times for Resolve are 291.2 ks for East and 293.2 ks for West, while those for Xtend are 242.0 ks for East and 250.8 ks for West. Among the five Resolve X-ray event grades (Y. Ishisaki et al. 2018), only the high-res events were used throughout this Letter, whose fraction was higher than 93% in the screened data for both observations.

The on-orbit time-dependent gain for each of the Resolve detector pixels was monitored and corrected using Mn Kα from the ^{55}Fe calibration sources on the FW using the standard XRISM/Resolve method described by F. S. Porter et al. (2024). There is a known anomalous behavior for pixel 27, and it was excluded in the spectral analysis. For each pixel, the measured line centroid shift and its statistical uncertainty after the drift correction are $\leqslant 0.05$ eV at 5.9 keV during the fiducial intervals with the FW ^{55}Fe sources. The Resolve detector also contains a calibration pixel that is part of the focal plane but located just outside of the instrument aperture and is illuminated continuously with a finely collimated ^{55}Fe source. We use the calibration pixel to monitor the efficacy of the time-dependent reconstruction of the energy scale during the main observation outside of the fiducial intervals. The reconstruction error was 0.39 and 0.11 eV at 5.9 keV for East and West, respectively. We add this in quadrature with an estimate of the observation-independent energy scale uncertainty obtained by using additional onboard calibration sources (M. E. Eckart et al. 2024) of 0.3 eV across the band 5.4–9.0 keV. This yields an energy scale uncertainty of 0.49 eV for East and 0.32 eV for West. In addition, the per-pixel and composite-array energy resolution were measured as 4.0–5.5 eV and 4.5 eV FWHM, respectively, at 5.9 keV for high-resolution events using the ^{55}Fe sources during the gain

---
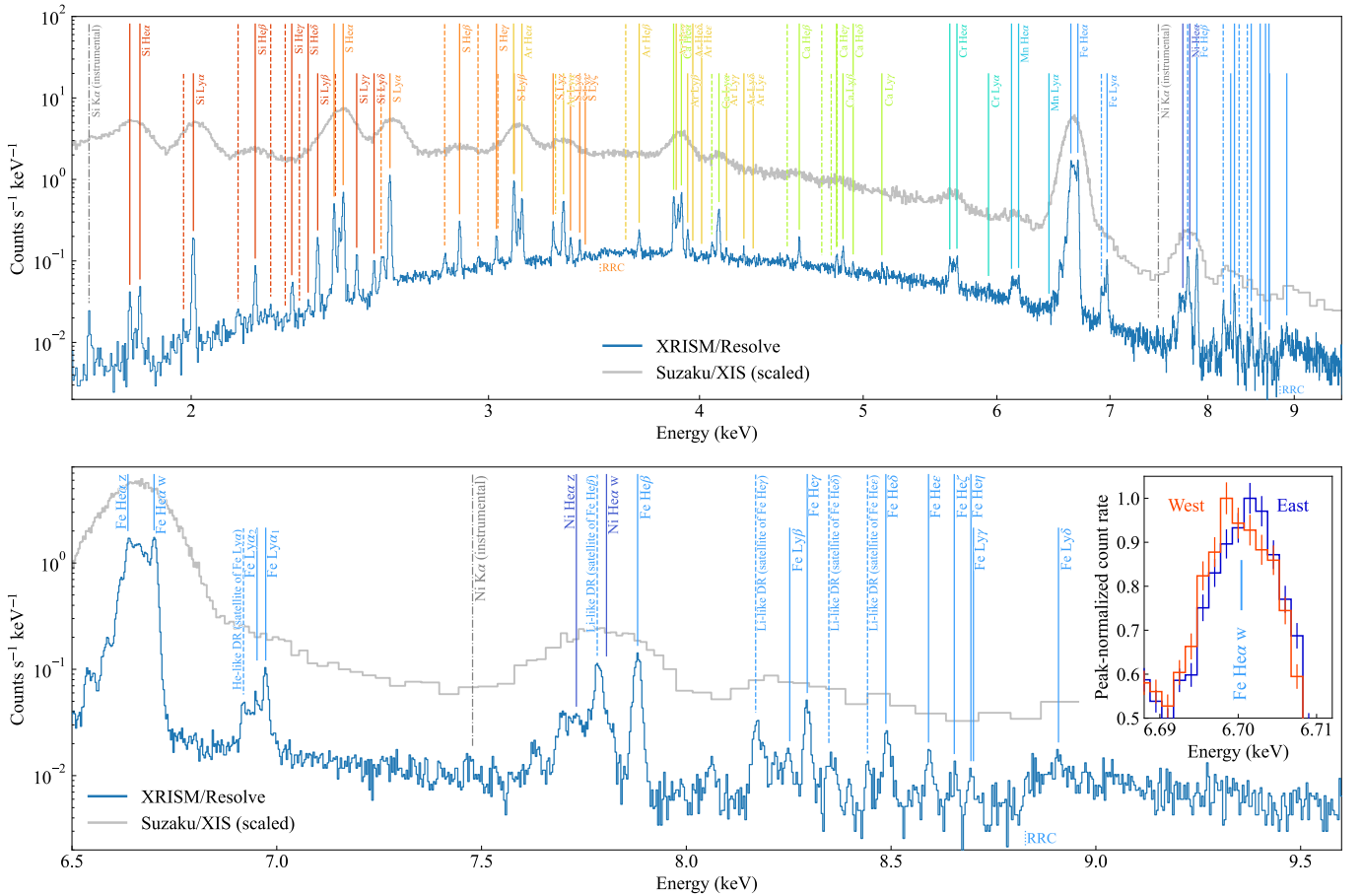
Figure 1. The integrated spectra of W49B with Resolve (blue histogram). Only the high-resolution events are included. Emission features from ions of different elements are labeled: solid lines for Rydberg series lines (Heα, Lyα, and higher-shell transition lines), dashed lines for DR satellite lines, and dotted lines for H-like S XV RRC and He-like Fe XXV RRC. Compared with the Resolve result is the spectrum with Suzaku X-ray Imaging Spectrometer (XIS; gray histogram) from M. Sawada et al. (2025). The inset in the bottom panel shows the close-up view of the Fe Heα line plotted for the two observations separately.

fiducial intervals.[63] The resolution was stable during the observations as monitored continuously using the calibration pixel. The per-pixel energy resolution uncertainty for Resolve has been measured on the ground and in flight and is energy dependent but corresponds to <0.15 eV FWHM at 6 keV and <0.3 eV at 10 keV.

3. Analysis and Results

3.1. Integrated Spectrum

We first examined the Resolve full-array spectrum merged for the two observations, shown in Figure 1. In the top panel, emission lines from ions of Si, S, Ar, Ca, Cr, Mn, and Fe are clearly resolved, with a possible underlying contribution from ions of other elements such as Ni. These spectral lines consist mainly of the strong Heα complex consisting of the $2p{\rightarrow}1s$ resonance and intercombination lines and the $2s{\rightarrow}1s$ forbidden line, known as lines w, x, y, and z, respectively. The hydrogen-like $2p{\rightarrow}1s$ Lyα doublets and higher-shell Rydberg transitions ($np{\rightarrow}1s$ with $n \geqslant 3$, denoted as Heβ, Heγ, etc., for He-like ions, for instance) and their dielectronic recombination (DR) satellite lines are also observed. Radiative recombination continuum (RRC) edges are clearly detected for Fe XXV at 8.8 keV and S XVI at 3.5 keV. As evident in the bottom panel,

the $n \geqslant 3$ Rydberg lines from He-like ions are detected at least up to $n = 8$ (Heη) in the case of Fe XXV, and these are accompanied with DR satellites of comparable intensities. Together with the strong RRC, high-n excitation lines and strong DR satellites are characteristics of a recombining plasma (J. S. Kaastra et al. 2008; M. Sawada et al. 2025), which is well showcased in the Resolve spectrum.

The inset in the bottom panel of Figure 1 is a close-up view of the peak-normalized Fe Heα resonance (w) lines from the two observation fields. Despite a large overlap of the observation fields at the bright center of the remnant, the resonance line peaks are slightly but significantly shifted and skewed in the opposite directions, redward for West and blueward for East. This indicates a systematic LOS velocity variation across the Fe ejecta. The peak energy difference is about two energy bins in the plot, or 3 eV, corresponding to a possible LOS velocity separation of ≈ 130 km s^{-1}.

3.2. Pixel-to-pixel Fe Heα Spectra

To examine the possible LOS velocity variation, we next analyzed pixel-to-pixel Resolve spectra. The projected locations of Resolve FOVs and pixel positions are shown with the Resolve and Xtend images of Fe Heα in Figure 2. The contours compared to these are from the Chandra Advanced CCD Imaging Spectrometer (ACIS) 6.3–7.0 keV map using

---

[63] https://heasarc.gsfc.nasa.gov/docs/xrism/analysis/gainreports/index.html
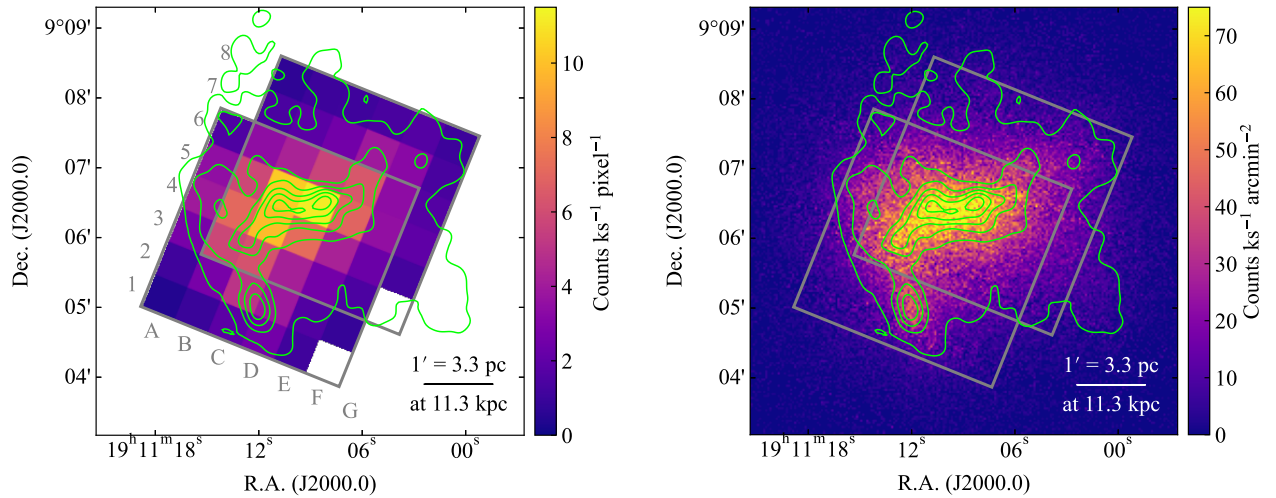
Figure 2. The XRISM Fe Heα band images of W49B with Resolve (left; in 6.53–6.80 keV) and Xtend (right; in 6.4–6.9 keV). The two large squares show the East and West Resolve FOVs. The contours are generated from Chandra's ACIS 6.3–7.0 keV. The Resolve image is affected by both the blurring due to the mirrors' PSF and the relatively sparse 6 × 6 detector array. In the Xtend, the spatial resolution is entirely determined by the mirror PSF.

4×4 binning and smoothed with a $4''$ Gaussian kernel. The image is from the Chandra Supernova Remnant Catalog.[64]

The two fields have significant overlap at the center of the remnant. Thus, in regions of the sky covered by both observations, we merged single-pixel spectra from the two fields into one spectrum. The alignment error of the pixel boundaries between the two fields was only $1''.2$. The redistribution matrix file (RMF) was generated for each pixel using the `rslmkrmf` tool. Throughout this Letter, the large-type RMF was used; hence, all the modeled detector-relevant matrix components except for the electron-loss continuum are included. This choice is appropriate for this study because we concentrate on the narrowband spectral fits where the electron-loss continuum component does not affect our results. For regions covered by both observations, an exposure-time-weighted average of the RMFs for each pixel pair was taken. For the auxiliary response file, we used the one simulated for on-axis point sources observed with the full array of Resolve. This would significantly overestimate the effective area when analyzing a single-pixel spectrum; however, it is appropriate here because the absolute normalization of the spectrum does not correlate with the LOS velocity or broadening. In other words, a possible systematic deviation in the relative effective area (or its energy dependence) arising from the assumption of a point-like source distribution instead of an extended source distribution is too small to alter fitting results in the narrowband analysis.

The Fe Heα spectrum from each Resolve pixel was fitted in the 6.53–6.80 keV range with the recombining plasma model `brnei` in the spectral fitting package Xspec (K. A. Arnaud 1996) with the atomic code AtomDB version 3.0.9 (R. K. Smith et al. 2001; A. R. Foster et al. 2012; A. R. Foster 2020). We note that switching the atomic code to the recently released AtomDB versions 3.1.0–3.1.2 or using an alternative spectral fitting package and atomic code SPEX version 3.08.01 (J. S. Kaastra et al. 1996; J. S. Kaastra et al. 2024) with its nonequilibrium ionization plasma model `neij` does not affect the results, discussions, or conclusions presented in this Letter. The model parameters are the emission measure (EM) as a

normalization of a spectrum, the electron temperature (kT_e), the initial temperature (kT_{init}) and recombination timescale (τ_{rec}) to give the overionized charge-state distribution, the abundance (Z), the redshift (z), and the velocity dispersion (σ_V) describing the line broadening. Note that the thermal broadening is not modeled because the ion temperature is unknown in an SNR where the electron–ion temperature equilibrium is not necessarily reached. The abundance (effectively the Fe abundance) was fixed at $5\times$ the solar values (K. Lodders et al. 2009) because the continuum level cannot be determined for some of the pixels with relatively low statistics. Also fixed during the fit was the initial temperature set at 4 keV (e.g., H. Yamaguchi et al. 2018).

Three examples of the spectral fits are shown in Figure 3. Each of these was taken from one Resolve detector pixel along the bright Fe ejecta bar. The dashed vertical lines in the spectral plots indicate the rest-frame energy of the Fe Heα-w line. The observed peaks show significant shifts by 5–6 eV. A blueshift is detected in a southeastern region (A2), while it is rather a redshift in a northwestern region (G8). The spectrum of the pixel located at the middle of the remnant (D5) appears to have almost no energy shift. It is also worth noting that the middle spectrum does not show a clear sign of double-peak structure, which would be expected toward the center of an expanding shell. Note that region A2 near the southeastern corner appears to be located outside the sharp limb in the Chandra 6.3–7.0 keV image but actually has significant counts from the limb due to the point-spread function (PSF) of XRISM's X-ray mirrors with a half-power diameter of $1'.3$ (T. Hayashi et al. 2024).

To have a full picture of the velocity structure, we derived pixel maps of the LOS velocity (obtained as $V_{LOS} = cz$, where c is the speed of light) and line broadening ($\sigma_E = \sigma_V E/c$, where E is the rest-frame energy of the resonance line of Fe Heα, 6700.42 eV) as in the left panels of Figure 4. Here the line broadening is expressed in the energy space rather than in the velocity space. This is because—unlike the line centroid shift, whose only possible astrophysical origin for a Galactic source is the LOS velocity—the broadening can also be contributed by nonkinematic factors such as thermal broadening. The LOS velocity shows a systematic gradient from blueshift

---
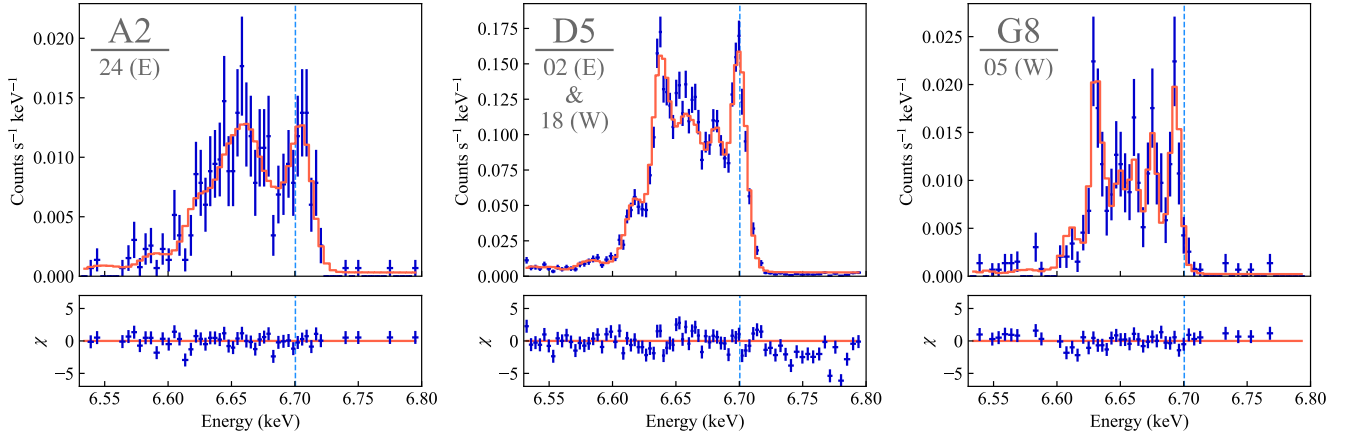
Figure 3. Examples of pixel-by-pixel Fe Heα spectral fits (top panels) from the A2, D5, and G8 regions (Figure 2) with residuals shown in the form of (data − model)/(1σ error) (bottom panels). The dashed vertical lines show the rest-frame energy of the Fe Heα resonance line (w), which corresponds to the highest-energy peak in the data shown. The numbers below the region name show the detector pixels used, E for East and W for West.
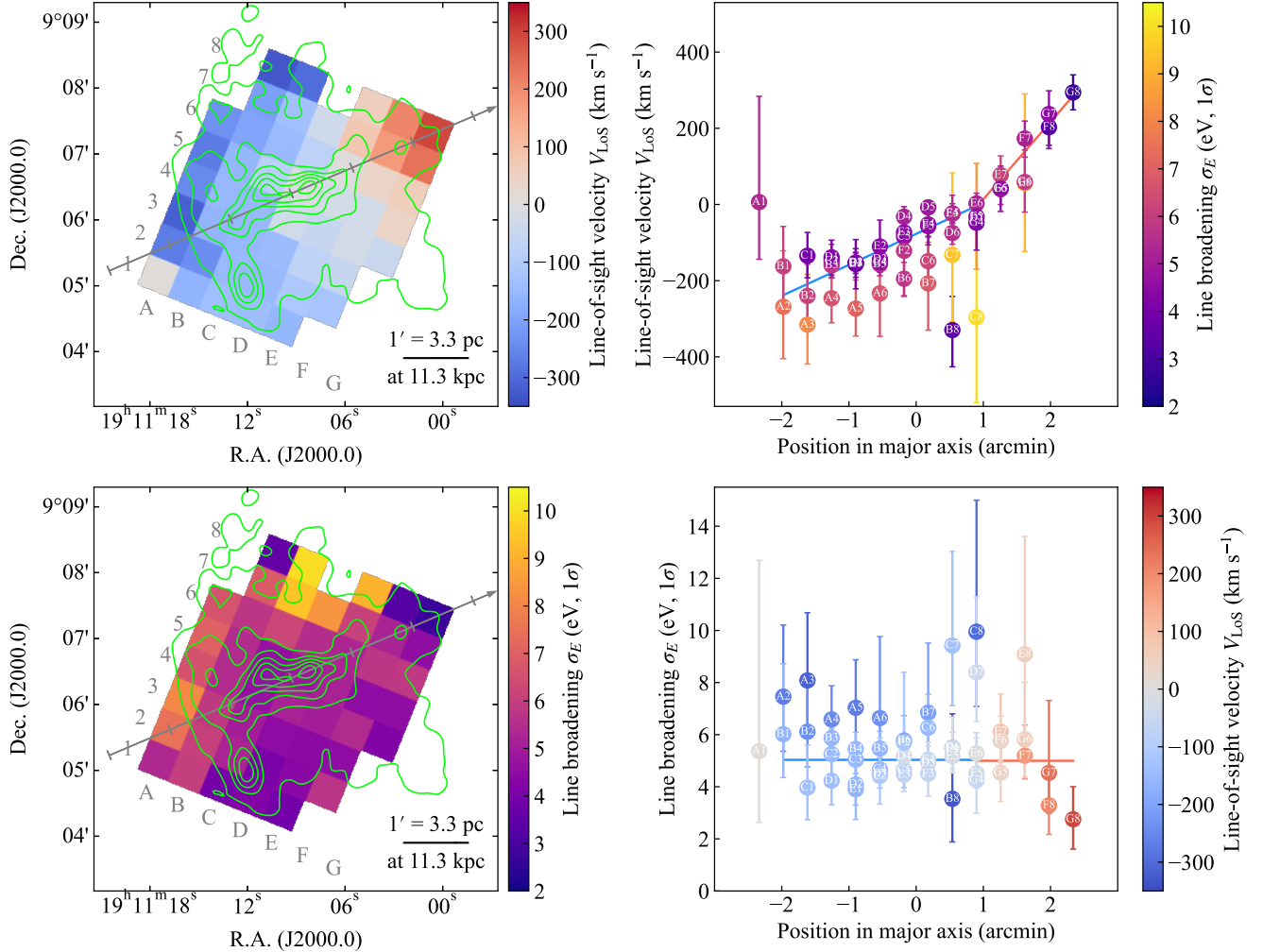
Figure 4. The LOS velocity (top) and line broadening (bottom) measured at Fe Heα. The left panels show pixel maps, with the ticked arrows tracing the approximate major axis of the Fe ejecta, while the right panels show values with the 90% statistical errors as a function of the position along the major axis.

(negative V_{LoS}) in the east to redshift (positive V_{LoS}) in the west. The map also shows that pixels with the larger blueshift values were found around the northern corner (such as B7 and B8 in Figure 2) and northeastern edge (such as A2–A6 and B2)

of the Resolve FOVs, indicating a local structure on top of the overall east–west gradient. On the other hand, the line broadening does not show the east–west gradient and seems to have a nearly constant value except a few edge regions to the

north. Those with the largest broadening (C7–C8, D7, and E8) lie between the boundary of the large blueshift and redshift regions, indicating that the large broadening may be the result of the relatively large PSF that causes a spatial mixing of the spectral components, i.e., spatial–spectral mixing (SSM) of different velocity components.

The LOS velocities and line broadenings are plotted in the right panels of Figure 4, each as a function of the position in the major axis of the Fe ejecta. The LOS velocity shows a nearly monotonic change along the major axis of the ejecta bar, confirming the east–west gradient. It appears that the gradient is steeper in the redshifted part in the west than in the blueshifted part in the east. By fitting a linear function to the $V_{\rm LOS}$ distribution in the top right panel of Figure 4, we derived the slope and intercept for redshifted and blueshifted groups as shown with solid lines. In this evaluation, we ignored A1, B8, and C8, as these are outliers. The outliers were identified by comparing $V_{\rm LOS}$ of each pixel to adjacent pixels along the major axis. Thus, evaluated local deviations in $V_{\rm LOS}$ were 220–250 km s^{-1} for these three pixels, while those for the remaining pixels were 130 km s^{-1} at largest and distributed in $\approx 60 \pm 40$ km s^{-1} (standard deviation). We note that exclusion of the outliers in this analysis does not significantly impact the results because of the large statistical errors. The slope for the redshifted group was 62 ± 9 km s^{-1} pc^{-1}, while that for the blueshifted group was 25 ± 3 km s^{-1} pc^{-1}, for the distance of 11.3 kpc. These differ significantly from each other by a factor of two. The slope derived including both groups was 32 ± 2 km s^{-1} pc^{-1}. The overall line broadening distribution, in contrast to the LOS velocity, shows no significant gradient with a best-fit slope of 0.035 ± 0.045 eV pc^{-1}. A search for the east–west difference was conducted also for the line broadening, but in this case using a constant model to compare the average broadenings. The two groups showed an identical average broadening of $\sigma_E = 5.0$ eV as shown with the solid lines in the bottom right panel of Figure 4. This corresponds to $\sigma_V = 220$ km s^{-1} if it is fully attributed to the velocity dispersion, or alternatively, an ion temperature of ≈ 30 keV for Fe if it is fully attributed to the thermal broadening. We note that the redshifted group showed an indication of a local gradient of -0.46 ± 0.23 eV pc^{-1}, which is a 3.3σ deviation from a constant broadening case. We emphasize that, with the resolution of 4.5 eV at FWHM (or 1.9 eV at 1σ), the major structures of the Fe Heα complex with $\sigma_E = 5$ eV are well resolved as in the middle panel of Figure 3, and therefore the lack of a gradient in the overall line broadening distribution is not because of insufficient sensitivity to detect enhanced broadening but because of the absence of a systematic gradient in the intrinsic broadening except for a possible local trend in the northwest.

In this pixel-by-pixel spectral analysis, the best-fit values of the thermal parameters were also obtained. Significant variations were found in the electron temperature, $kT_e = 1.1–1.7$ keV, and in the recombination timescale, $\tau_{\rm rec} = (1–6) \times 10^{11}$ cm^{-3} s. These are in good agreement with the previous studies (e.g., H. Yamaguchi et al. 2018). The detailed results on the thermal parameters and their spatial distributions will be presented elsewhere.
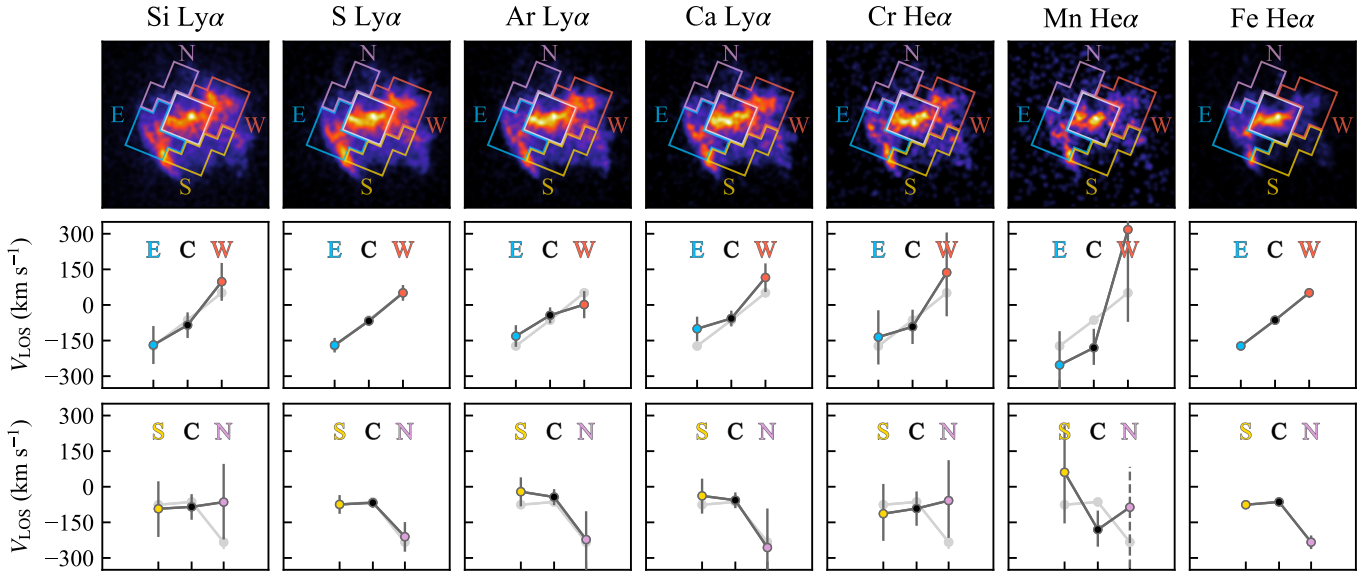
3.3. LOS Velocity of Various Elements

The spatial distribution of ejecta is systematically different between elements (R. Fujimoto et al. 1995; J. W. Keohane

et al. 2007). It is natural for one to expect that such a difference exists also in the velocity distribution. Because the statistics of other lines are limited compared to Fe Heα, we grouped Resolve detector pixels to compose five regions covering the center (C), north (N), south (S), east (E), and west (W) of the remnant and analyzed their spectra in several narrow energy bands, encompassing Lyα lines of Si, S, Ar, and Ca and Heα of Cr, Mn, and Fe. Note that, among the 49 pixel regions analyzed in Section 3.2, the five pixel regions in row 1 in Figure 4 were excluded in this analysis to make the locations of the E and W regions with respect to the C region more symmetric. The preference of H-like Lyα to Heα for intermediate-mass elements (Si, S, Ar, and Ca) is because Lyα is comparably bright to Heα and is relatively free from mixing with lines of other elements; e.g., Heα of S and Ar are overlapping with a DR satellite of Si and Lyβ of S, respectively, as seen in Figure 1. The preference of Heα to Lyα for Fe-group elements (Cr, Mn, and Fe) is because Lyα is much fainter. We thus chose the energy bands to be 1.99–2.03 keV for Si, 2.60–2.64 keV for S, 3.30–3.34 keV for Ar, 4.08–4.14 keV for Ca, 5.55–5.75 keV for Cr, 6.05–6.25 keV for Mn, and 6.53–6.80 keV for Fe.

We first performed a baseline fit for each region in 6.53–7.02 keV covering both Fe Heα and Fe Lyα to determine the thermal parameters and the EM, and then we analyzed individual narrowband spectra to determine the LOS velocities and line broadenings. The reason why the continuum was not adopted in the determination of the thermal parameters in the baseline fit is mainly because it would be complicated by the presence of the non-X-ray background, while we confirmed that the changes in the thermal parameters by including the continuum in the 5.0–7.5 keV band but excluding the Cr and Mn Heα lines are not significant ($\approx 1\sigma$ at largest) even without properly modeling the non-X-ray background. In both analysis steps, we used bvvrnei in place of brnei to allow elemental abundance to have separate values depending on elements. We also employed tbabs to reproduce the interstellar absorption at low energies assuming an atomic hydrogen equivalent column density of 5×10^{22} cm^{-2} (J. W. Keohane et al. 2007). In the baseline fit, we set the initial temperature at 4 keV as in the pixel-by-pixel analysis (Section 3.2) and made the iron abundance free in addition to the five free parameters (EM, kT_e, $\tau_{\rm rec}$, z, and σ_V). The best-fit thermal parameters in the baseline fit were all within the ranges of the variations found in the pixel-by-pixel analysis of Fe Heα (Section 3.2). In the individual fits, we fixed the three thermal parameters (kT_e, $kT_{\rm init}$, and $\tau_{\rm rec}$) and EM to those in the baseline fit, while making the other parameters free (z, σ_V, and the abundance of the element of interest). We note that modifying the thermal parameters within ranges of possible spatial or energy band dependence does not affect the measured LOS velocities significantly. For instance, if we take the Si Lyα fit of the C region as an example, we get only a small change of 10 km s^{-1} in the LOS velocity corresponding to the 0.3σ significance level, even with a drastic change of kT_e from 1.5 keV with the baseline fit to 0.5 keV suggested as a low-temperature component partly contributing to the Si K band based on wide-band CCD spectroscopy (e.g., T. Holland-Ashford et al. 2020).

The LOS velocity $V_{\rm LOS}$ measured with the seven elements is shown in Figure 5. An immediate result is that the same east–west gradient as found in the pixel-by-pixel analysis of Fe Heα

Figure 5. The results of the LOS velocity V_{LOS} for various elements. The top panels show the five groups of the Resolve detector pixels with Chandra images (Si Lyα in 1.92–2.12 keV, S Lyα in 2.58–2.78 keV, Ar Lyα in 3.26–3.48 keV, Ca Lyα in 4.05–4.29 keV, Cr Heα in 5.45–5.90 keV, Mn Heα in 5.90–6.30 keV, and Fe Heα in 6.30–7.00 keV). The middle and bottom panels show the V_{LOS} variations along the east–west and north–south directions, respectively. The darker error bar plots are the results of the entitled energy bands, while the lighter-colored error bars behind them are those for Fe Heα for comparison. The errors are quoted at the 90% confidence level except for the one with a dashed bar, which is at the 68% level. See text for details.

is confirmed with all the elements (middle panels). There is a hint of a small variation between elements, e.g., Mn may have a larger blueshift in regions E and C and a larger redshift in region W compared to Fe, but these are statistically marginal. In the north–south direction (bottom panels), the change is not as monotonic as in the east–west direction. Regions C and S both show a mild blueshift with $V_{\mathrm{LOS}} \approx -70$ km s^{-1}, while region N shows a larger blueshift of $V_{\mathrm{LOS}} \approx -230$ km s^{-1} at Fe Heα, with which the other elements show consistent values within the statistical errors. The blueshift in region N is even greater than that in region E. This trend is consistent with the pixel-by-pixel analysis results (Figure 4, top left panel), where we found pixels with the largest blueshift at the northeastern edges. We note that, for Mn in region N, the 68% error is shown because the significance of the emission is too low to determine the 90% error.

4. Discussion

4.1. Kinematics of Ejecta in W49B

We first discuss the kinematics of the ejecta in W49B based on the LOS velocity and broadening measurements. The elongated bar-like morphology of the Fe ejecta is a unique feature of this remnant, which gives rise to various interpretations. In terms of the kinematics, these are broadly divided into two models. In one model, the ejecta are assumed to have bipolar flows along the major axis and the jetlike morphology is due to this intrinsic asphericity (J. W. Keohane et al. 2007; L. A. Lopez et al. 2013; D. F. González-Casanova et al. 2014). In the other model, the morphology is rather attributed to the enhanced reverse shock due to an aspherical circumstellar matter (CSM) or molecular cloud (M. Miceli et al. 2006, 2008; T. Shimizu et al. 2012; P. Zhou & J. Vink 2018), which may be supported by the existence of shock-excited clouds (e.g., P. Zhou et al. 2022). In this case, the motion of the ejecta should be dominated by a spherical or equatorial expansion of

disklike shocked ejecta. These two kinematic models are summarized in Figure 6.

We argue that the expanding disk model (Figure 6, left panel) is rejected by the presented measurements with XRISM. In this model, both the redshifted and blueshifted components should be seen along the ejecta bar, with the maximum LOS velocities at the center and the minimum at both ends. This expectation clearly contradicts the measured LOS velocity distribution (Figure 4, top right panel). The spectrum observed near the center of the remnant does not show a line splitting or double-peaked profile originating from the redshifted and blueshifted components (Figure 3, middle panel). One may argue that the line profile may depend on the radial distribution of the EM and velocity, i.e., if the density is higher toward the inner radii as suggested by the centrally peaked X-ray morphology and the expansion is homologous, then the emission lines may still have a single-peaked profile. In such a case, large LOS velocity components corresponding to the outer part of the expanding disk contribute to the broadening of the lines. Then, because the magnitude of the overall LOS velocity decreases toward the eastern and western ends of the ejecta, we would observe a monotonic decrease in the broadening outward. However, our measurement showed that the line broadening at Fe Heα is nearly uniform (Figure 4, bottom right panel).

The bipolar flows, on the other hand, naturally explain the observed LOS velocity distribution (Figure 6, right panel). If bipolar flows are slightly angled as in the schematic, the emission from the approaching side to us shifts blueward and that from the receding side from us shifts redward, reproducing the systematic difference in V_{LOS} between the eastern and western parts (Figure 4, top right panel). The smooth gradient in the LOS velocity can be explained if the bipolar flows are homologous, i.e., $V_r \sim r/t_{\mathrm{age}}$, where r is the radial (projected) distance from the SNR center, V_r is the radial (or projected) velocity, and t_{age} is the SNR age. The inclination angle of outflows with respect to the LOS direction is
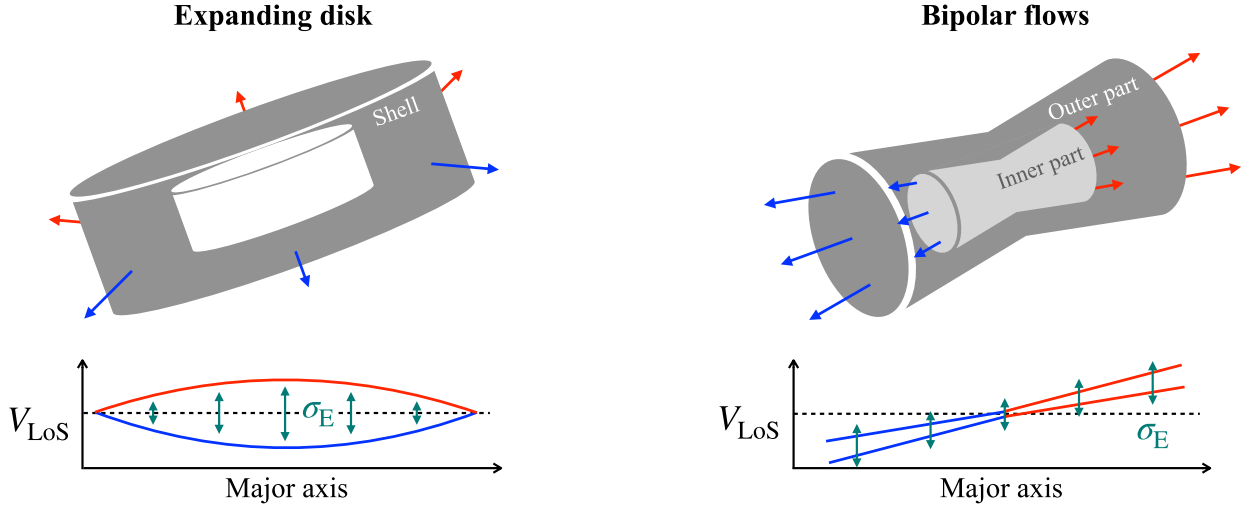
Figure 6. A schematic of the expected LOS velocity and broadening distributions for the two representative cases of the ejecta kinematics: equatorially expanding disk (left) and bipolar flows (right). The data and accompanying analysis presented here reject the expanding disk model.

$\theta \approx V_{\mathrm{LOS}}/V_r = V_{\mathrm{LOS}} t_{\mathrm{age}}/r$, which is

$$\theta \quad (\circ) \approx 6 \left(\frac{V_{\mathrm{LOS}}}{100 \text{ km s}^{-1}} \right) \left(\frac{r}{1 \text{ pc}} \right)^{-1} \left(\frac{t_{\mathrm{age}}}{10^3 \text{ yr}} \right). \quad (1)$$

For the estimated age of $t_{\mathrm{age}} \sim 5$ kyr (U. Hwang et al. 2000; P. Zhou & J. Vink 2018) and the LOS velocity of 300 km s^{-1} at the outermost part at $r = 6.6$ pc (semimajor axis), we get $\theta \approx 14°$. If we derive the inclination angle separately for the blueshifted and redshifted regions using the best-fit slopes (top right panel of Figure 4), $V_{\mathrm{LOS}}/r = 25$ and 62 km s^{-1} pc^{-1}, respectively (Section 3.2), it is slightly shallower ($\theta \approx 8°$) for the east and deeper ($\theta \approx 19°$) for the west.

We note that the smooth gradient in the LOS velocity is not due to the SSM, by which spectral components arising from spatially different locations are mixed owing to the PSF of the mirrors. If the actual LOS velocity distribution consists of two distinct groups of blueshift and redshift without having the intermediate group with almost no LOS velocity, then the nearly zero energy shift observed toward the center is due to a mixing of the blueshifted and redshifted components. As already discussed for the expanding disk model, with such a mixing we expect an enhancement of the broadening toward the center, which is not the case. Therefore, the smooth gradient cannot be explained by two distinct velocity groups affected by the SSM effect and should be an intrinsic property. This view is consistent with a nearly uniform broadening observed along the ejecta bar because the magnitude of the broadening due to the SSM effect is determined by the gradient of the LOS velocity, which is nearly constant. However, the velocity dispersion, obtained if the broadening (mostly 3–7 eV) is fully attributed to kinematic origins, is $\approx 220 \pm 90$ km s^{-1}, which is larger than the scale of the LOS velocity variation (100–200 km s^{-1}) within the half-power diameter of the PSF ($\sim 1'$), suggesting a significant contribution from other origins such as the thermal motion of ions. Distinguishing the origin of the broadening requires further analysis considering the SSM effect and will be reported elsewhere.

4.2. Implications for the Origin of W49B

We next discuss possible origins of W49B. As concluded in Section 4.1, the bipolar velocity distribution cannot be reproduced with spherically or equatorially expanding, disklike ejecta. This fact actually rejects most of the scenarios previously proposed.

4.2.1. Scenarios Predicting Equatorially Expanding Ejecta

P. Zhou & J. Vink (2018) proposed an asymmetric Type Ia model to simultaneously explain the abundance pattern and spatial distribution of heavy elements. In their model, the bar-like morphology was attributed rather to the anisotropy in the ambient mass density, which was assumed to be higher in the equatorial, east–west direction. This resulted in earlier and stronger reverse-shock formation in the east–west direction compared to the north–south direction. This is similar to the model considered by M. Miceli et al. (2006, 2008). In such a case, however, the expected kinematics should be an equatorially expanding disk (Figure 6 left), which is inconsistent with the observed V_{LOS} distribution with XRISM (Section 4.1).

A spherical core-collapse (CC) origin would be the next candidate (U. Hwang et al. 2000; L. Sun & Y. Chen 2020; M. Sawada et al. 2025) in terms of the elemental abundances. T. Shimizu et al. (2012) reproduced the bar-like X-ray morphology and the recombining plasma in their numerical simulations of a spherical CC explosion inside an axially symmetric, disklike CSM. In this scenario, the structure of the ejecta is an equatorially expanding disk (Figure 6, left panel), which is again inconsistent with the observed V_{LOS} distribution with XRISM (Section 4.1).

The recently proposed common-envelope jet SN scenario (A. Grichener & N. Soker 2023) considers a thermonuclear outburst in a massive accretion disk around a neutron star, formed by tidal disruption of the core of a companion red supergiant. This model explains both the Type Ia–like nucleosynthesis and the bar-like ejecta distribution. However, in this model the ejecta originate from the accretion disk rather than the bipolar jets launched in the direction perpendicular to it. The expected LOS velocity distribution of the ejecta,

therefore, should be closer to that of an equatorially expanding disk (Figure 6 left), which is clearly inconsistent with the XRISM result.

There are some scenarios that do not specify a particular explosion type or a progenitor mass. One of these is a model by G.-Y. Zhang et al. (2019), where an SNR was assumed to evolve in an ambient medium filled by many clumps of molecular clouds. While the kinematics of the ejecta may be altered by collisions with the dense clumps, it is unlikely that the cloud interaction acts to align the ejecta velocity to make bipolar flows. Therefore, even if the interaction plays a significant role in reproducing other observational characteristics of W49B, there must be another mechanism responsible for bipolar flows.

4.2.2. Bipolar SN Explosion

A certain type of massive star is expected to undergo jet-driven bipolar explosions (e.g., K. Maeda & K. Nomoto 2003), which have been proposed to be the cause of the bar-like morphology (J. W. Keohane et al. 2007; L. A. Lopez et al. 2013). The XRISM discovery of the bipolar kinematics (Figure 6, right panel) can easily be associated with this scenario. We note that, unlike the previous proposal by L. A. Lopez et al. (2013), a bipolar CC SN does not necessarily mean a hypernova origin. For instance, evidence for bipolar explosions in Type IIP SNe have been reported recently (T. Nagao et al. 2024).

A numerical simulation showed that, in this model, the bar-like structure is more prominent in Fe, while the more circular component is brighter in lighter elements such as Si and S (D. F. González-Casanova et al. 2014), which matches well with the observed morphologies in various energy bands. This may seem to contradict the common LOS velocity structures between elements (Section 3.3). We argue that this is not necessarily the case. For instance, in the simulations by D. F. González-Casanova et al. (2014), the more circular morphology of the lighter elements such as Si and S was due to their farther distributions from the jet axis rather than the lack of the bipolarity. These elements actually share the same bipolarity as Fe; therefore, we can expect similar LOS velocity distributions, especially with the spatial resolution of Resolve. We note that D. F. González-Casanova et al. (2014) simulated the evolution only up to 700 yr based on an old age estimate by J. P. Pye et al. (1984), which relied on the existence of synchrotron X-ray emission and is therefore no longer valid. The reproducibility of the bar-like structure at the age of W49B needs to be confirmed with a longer simulation time.

One may dispute the jet-driven bipolar explosion model because the jet base should be displaced to make a clear "gap" at the center of the remnant, which appears to be in contrast to the centrally peaked X-ray distribution in the Xtend image (Figure 2, right panel). However, in the finer-resolution Chandra image (contours in Figure 2), two bright spots near the center are evident, one at pixel region D5 and the other between pixel regions C4 and C5. These spots are connected with fainter emission filling the "gap." This emission can be explained by a projection effect as seen in the simulated X-ray maps by D. F. González-Casanova et al. (2014). The jet base has extended ring-like structures at outer radii of the jet axis. These structures of the two sides are superposed along the LOS at the center to produce X-rays from the "gap." The separation of the bright spots is $\approx 0.\!'6$ or ≈ 2 pc at 11.3 kpc,

indicating an average velocity of the jet base of ≈ 190 km s^{-1}. Assuming an inclination of $14°$ (Section 4.1), the separation in the LOS velocity is expected to be ≈ 90 km s^{-1}, which is consistent with the observed separation between these pixel regions (Figure 4). This also produces a sufficiently small line centroid splitting ($\lesssim 2$ eV) not to cause significant distortion or broadening in the observed spectrum at the center. Assuming that we interpret the two bright spots as the jet base, the jet center has an LOS velocity of ≈ -50 km s^{-1}, which is consistent with the fact that a larger fraction of the ejecta shows blueshift (Figure 4). The asymmetry may be caused by momentum taken away by the undiscovered central compact object, suggesting its runaway direction toward the west. We note that the X-ray distribution in the simulations by D. F. González-Casanova et al. (2014) still has some discrepancies from the observed one, such as the jet tip being brighter than the jet base as opposed to the observation.

The bipolar SN with massive progenitor scenario, however, does not support other aspects of this SNR, mainly the elemental abundances, such as the high Mn and low Ti abundances (P. Zhou & J. Vink 2018; T. Sato et al. 2025). A recent spectroscopic study with Suzaku showed that the abundance ratio measurements of the Fe-group elements, especially Ni/Fe, depended on the choice of the atomic codes (M. Sawada et al. 2025). Together with other systematics originating from the moderate energy resolution of X-ray CCDs, it is possible that the previously reported results are biased. High-resolution spectroscopy is imperative to get decisive results. The feasibility of the massive progenitor bipolar explosion scenario will be revisited in a separate paper with updated abundance measurements with XRISM/Resolve.

Bipolarity is not necessarily a unique feature to CC SNe but could also be achieved by highly asymmetric Type Ia SNe. One possibility is a gravitationally confined detonation model (T. Plewa et al. 2004; D. M. Townsley et al. 2007; G. C. Jordan et al. 2008). In this scenario, once off-center ignitions are triggered, deflagration propagates in one direction to break through the stellar surface and then spreads rapidly over the stellar surface to collide at the opposite point from the break out point, resulting in a pair of outwardly and inwardly directed jets. Therefore, along the jet axis, the bipolar structure should have the same direction, which is inconsistent with the LOS velocity structure observed in W49B. Another possibility is a rapid, differential rotation of a progenitor white dwarf, which is considered to be a possible origin for a superluminous Type Ia SN (M. Fink et al. 2018). In this scenario, bipolar flows of ejecta developing in opposite directions are expected and therefore are in a fair agreement with our observations.

4.2.3. Ejecta Evolving in Bipolar CSM

Bipolar ejecta flows may alternatively be produced by the interaction of initially symmetric ejecta with dense CSM, as was the case for some of the scenarios discussed in Section 4.2.1. To make bipolar flows, the structure of dense CSM needs to be bipolar rather than disklike or torus-like.

A simulation geometrically similar to a bipolar CSM case was performed by X. Zhou et al. (2011), where a barrel-shaped dense ring around the explosion center was employed. In the simulation, it was shown that ejecta were collimated by the ring and formed an elongated structure along the symmetry axis of the ring. The combined effect of the heating of inner ejecta by the reflected shock from the ring and cooling of outer

ejecta by mixing with cooler plasma produced by an evaporated cloud from the ring caused an enhanced EM at the center. Moreover, the collimation also forces ejecta flows to be aligned with the ring's symmetry axis, making bipolar kinematics qualitatively similar to those observed with XRISM. The choice of the barrel-shaped ring was motivated by the coaxial rings of CSM observed in the infrared and radio wavelengths, whose physical origin was speculated to be bipolar winds from a massive progenitor star (C. K. Lacey et al. 2001; J. W. Keohane et al. 2007). However, recent abundance measurements instead suggested a Type Ia origin for W49B (e.g., P. Zhou & J. Vink 2018; T. Sato et al. 2025).

We propose that such a dense, bipolar CSM may be realized by a recently formed planetary nebula (T. Court et al. 2024). Indeed, such a CSM structure, viewed from the polar direction, was discovered in the SNR N103B as double rings (H. Yamaguchi et al. 2021). If a similar CSM structure existed for a progenitor of W49B, it may have shaped bipolar flows of hot plasma as the ejecta expanded inside the bipolar cavity and formed the bar-like X-ray morphology in the edge-on view as simulated by X. Zhou et al. (2011). If this is indeed the case, then the existence of a binary companion star to the progenitor of W49B may be suggested because binary interactions are considered to be a preferred channel to form a bipolar planetary nebula (O. De Marco 2009; D. Jones & H. M. J. Boffin 2017).

A bipolar CSM may alternatively be realized in a CC scenario by a massive progenitor. For instance, a luminous blue variable may form a bipolar CSM, and even if its explosion is spherical, a jetlike, bipolar structure of the ejecta may be developed, as simulated by S. Ustamujic et al. (2021). Wolf−Rayet stars may also develop bipolar CSM (D. M. A. Meyer 2021). With a massive progenitor ($\gtrsim 30\,M_{\odot}$), a large wind-blown bubble of $\gtrsim 20$ pc is likely formed during its main-sequence phase. The small size of ≈ 5 pc of the wind-blown bubble suggested in W49B was previously argued to be the evidence against such a very massive progenitor (P. Zhou & J. Vink 2018), while the existence of the wind-blown bubble in this remnant is still debated (J. Siegel et al. 2020).

The CSM cavity as the primary origin of the bipolar flows is also consistent with the commonality of the LOS velocity structures between elements (Section 3.3), although the intrinsic elemental distribution in the ejecta may still cause some differences (S. Ustamujic et al. 2021). The bipolar CSM may have caused the rarefaction of the plasma by the same mechanism as H. Itoh & K. Masai (1989), which may also explain the recombining plasma. Indeed, in the simulation by X. Zhou et al. (2011), the inner ejecta that were once hot and dense owing to the reflection shock underwent rapid adiabatic expansion in the later stage of evolution, which, in combination with mixing of evaporated cloud materials, made an overionized charge-state distribution.

5. Summary

In this work we have presented the first ever high-resolution X-ray spectroscopy for the Galactic SNR W49B using the Resolve microcalorimeter spectrometer on XRISM. The spectrum is full of emission lines, including high-shell transition lines and DR satellite lines, which are the characteristics of a recombining plasma.

We have investigated the LOS velocity structure of the ejecta using strong lines from various elements. The Fe Heα lines are sufficiently bright to perform the pixel-by-pixel

velocity measurements. In the pixel map, the overall LOS velocity distribution is characterized by a smooth gradient along the major axis of the ejecta bar, connecting the blueshift in the east and the redshift in the west, with a maximum magnitude of $\sim 300\,\mathrm{km\,s^{-1}}$. An asymmetry is found in the gradient between the redshifted and blueshifted parts of the ejecta, indicating a possible influence of the ambient density or an intrinsic inclination difference. The elemental dependence of the LOS velocity structure has been examined with spectra extracted from larger regions dividing the SNR into five parts, finding no significant variations.

The observed LOS velocities and the broadening are inconsistent with an expanding disk model, which is expected for most of the scenarios that assume a spherical explosion. An exceptional case would be one exploding and evolving in a dense CSM with a bipolar structure, which may be expected, for instance, from a Type Ia SN that exploded inside a bipolar planetary nebula. In such a case where the CSM plays a significant role in shaping the bipolar ejecta flows, the observed common velocity structures between elements would also be explained easily. A bipolar SN explosion would also explain the kinematics observed with XRISM, while a bipolar CC SN would not be favored in terms of the elemental abundance pattern, as previously pointed out. The XRISM spectrum presented in this Letter is also suitable for accurately measuring the elemental abundances, in particular of the Fe-group elements. Hence, these data could potentially resolve this controversy. That work is left to a future publication.

ORCID iDs

Marc Audard ⓘ https://orcid.org/0000-0003-4721-034X
Hisamitsu Awaki ⓘ https://orcid.org/0000-0001-7204-4350
Ralf Ballhausen ⓘ https://orcid.org/0000-0002-1118-8470
Aya Bamba ⓘ https://orcid.org/0000-0003-0890-4920
Ehud Behar ⓘ https://orcid.org/0000-0001-9735-4873
Rozenn Boissay-Malaquin ⓘ https://orcid.org/0000-0003-2704-599X
Laura Brenneman ⓘ https://orcid.org/0000-0003-2663-1954
Gregory V. Brown ⓘ https://orcid.org/0000-0001-6338-9445
Lia Corrales ⓘ https://orcid.org/0000-0002-5466-3817
Elisa Costantini ⓘ https://orcid.org/0000-0001-8470-749X
Renata Cumbee ⓘ https://orcid.org/0000-0001-9894-295X
María Díaz Trigo ⓘ https://orcid.org/0000-0001-7796-4279
Chris Done ⓘ https://orcid.org/0000-0002-1065-7239
Ken Ebisawa ⓘ https://orcid.org/0000-0002-5352-7178
Megan E. Eckart ⓘ https://orcid.org/0000-0003-3894-5889
Dominique Eckert ⓘ https://orcid.org/0000-0001-7917-3892
Satoshi Eguchi ⓘ https://orcid.org/0000-0003-2814-9336
Teruaki Enoto ⓘ https://orcid.org/0000-0003-1244-3100
Adam Foster ⓘ https://orcid.org/0000-0003-3462-8886
Ryuichi Fujimoto ⓘ https://orcid.org/0000-0002-2374-7073
Yutaka Fujita ⓘ https://orcid.org/0000-0003-0058-9719
Yasushi Fukazawa ⓘ https://orcid.org/0000-0002-0921-8837
Kotaro Fukushima ⓘ https://orcid.org/0000-0001-8055-7113
Luigi Gallo ⓘ https://orcid.org/0009-0006-4968-7108
Javier A. García ⓘ https://orcid.org/0000-0003-3828-2448
Liyi Gu ⓘ https://orcid.org/0000-0001-9911-7038
Matteo Guainazzi ⓘ https://orcid.org/0000-0002-1094-3147
Kouichi Hagino ⓘ https://orcid.org/0000-0003-4235-5304
Kenji Hamaguchi ⓘ https://orcid.org/0000-0001-7515-2779
Isamu Hatsukade ⓘ https://orcid.org/0000-0003-3518-3049
Katsuhiro Hayashi ⓘ https://orcid.org/0000-0001-6922-6583
Takayuki Hayashi ⓘ https://orcid.org/0000-0001-6665-2499
Natalie Hell ⓘ https://orcid.org/0000-0003-3057-1536
Edmund Hodges-Kluck ⓘ https://orcid.org/0000-0002-2397-206X
Ann Hornschemeier ⓘ https://orcid.org/0000-0001-8667-2681
Yuto Ichinohe ⓘ https://orcid.org/0000-0002-6102-1441
Yoshitaka Ishisaki ⓘ https://orcid.org/0000-0003-0163-7217
Jelle Kaastra ⓘ https://orcid.org/0000-0001-5540-2822
Timothy Kallman ⓘ https://orcid.org/0000-0002-5779-6906
Erin Kara ⓘ https://orcid.org/0000-0003-0172-0854
Satoru Katsuda ⓘ https://orcid.org/0000-0002-1104-7205
Yoshiaki Kanemaru ⓘ https://orcid.org/0000-0002-4541-1044
Richard L. Kelley ⓘ https://orcid.org/0009-0007-2283-3336
Caroline A. Kilbourne ⓘ https://orcid.org/0000-0001-9464-4103
Shunji Kitamoto ⓘ https://orcid.org/0000-0001-8948-7983
Shogo Kobayashi ⓘ https://orcid.org/0000-0001-7773-9266
Takayoshi Kohmura ⓘ https://orcid.org/0000-0003-4403-4512
Maurice A. Leutenegger ⓘ https://orcid.org/0000-0002-3331-7595
Michael Loewenstein ⓘ https://orcid.org/0000-0002-1661-4029
Yoshitomo Maeda ⓘ https://orcid.org/0000-0002-9099-5755
Maxim Markevitch ⓘ https://orcid.org/0000-0003-0144-4052
Kyoko Matsushita ⓘ https://orcid.org/0000-0003-2907-0902
Dan McCammon ⓘ https://orcid.org/0000-0001-5170-4567
Brian McNamara ⓘ https://orcid.org/0000-0002-2622-2627
François Mernier ⓘ https://orcid.org/0000-0002-7031-4772
Eric D. Miller ⓘ https://orcid.org/0000-0002-3031-2326
Jon M. Miller ⓘ https://orcid.org/0000-0003-2869-7682
Ikuyuki Mitsuishi ⓘ https://orcid.org/0000-0002-9901-233X
Misaki Mizumoto ⓘ https://orcid.org/0000-0003-2161-0361
Tsunefumi Mizuno ⓘ https://orcid.org/0000-0001-7263-0296
Koji Mori ⓘ https://orcid.org/0000-0002-0018-0369
Koji Mukai ⓘ https://orcid.org/0000-0002-8286-8094
Richard Mushotzky ⓘ https://orcid.org/0000-0002-7962-5446
Hiroshi Nakajima ⓘ https://orcid.org/0000-0001-6988-3938
Kazuhiro Nakazawa ⓘ https://orcid.org/0000-0003-2930-350X
Jan-Uwe Ness ⓘ https://orcid.org/0000-0003-0440-7193
Kumiko Nobukawa ⓘ https://orcid.org/0000-0002-0726-7862
Masayoshi Nobukawa ⓘ https://orcid.org/0000-0003-1130-5363
Hirofumi Noda ⓘ https://orcid.org/0000-0001-6020-517X
Shoji Ogawa ⓘ https://orcid.org/0000-0002-5701-0811
Anna Ogorzalek ⓘ https://orcid.org/0000-0003-4504-2557
Takashi Okajima ⓘ https://orcid.org/0000-0002-6054-3432
Naomi Ota ⓘ https://orcid.org/0000-0002-2784-3652
Stephane Paltani ⓘ https://orcid.org/0000-0002-8108-9179
Robert Petre ⓘ https://orcid.org/0000-0003-3850-2041
Paul Plucinsky ⓘ https://orcid.org/0000-0003-1415-5823
Frederick S. Porter ⓘ https://orcid.org/0000-0002-6374-1119
Katja Pottschmidt ⓘ https://orcid.org/0000-0002-4656-6881
Hidetoshi Sano ⓘ https://orcid.org/0000-0003-2062-5692
Kosuke Sato ⓘ https://orcid.org/0000-0001-5774-1633
Toshiki Sato ⓘ https://orcid.org/0000-0001-9267-1693
Makoto Sawada ⓘ https://orcid.org/0000-0003-2008-6887
Megumi Shidatsu ⓘ https://orcid.org/0000-0001-8195-6546
Aurora Simionescu ⓘ https://orcid.org/0000-0002-9714-3862
Randall Smith ⓘ https://orcid.org/0000-0003-4284-4167
Hiromasa Suzuki ⓘ https://orcid.org/0000-0002-8152-6172
Andrew Szymkowiak ⓘ https://orcid.org/0000-0002-4974-687X
Hiromitsu Takahashi ⓘ https://orcid.org/0000-0001-6314-5897
Toru Tamagawa ⓘ https://orcid.org/0000-0002-8801-6263
Keisuke Tamura ⓘ https://orcid.org/0009-0004-7101-4503
Takaaki Tanaka ⓘ https://orcid.org/0000-0002-4383-0368
Atsushi Tanimoto ⓘ https://orcid.org/0000-0002-0114-5581
Makoto Tashiro ⓘ https://orcid.org/0000-0002-5097-1257
Yukikatsu Terada ⓘ https://orcid.org/0000-0002-2359-1857
Yuichi Terashima ⓘ https://orcid.org/0000-0003-1780-5481
Yohko Tsuboi ⓘ https://orcid.org/0000-0001-9943-0024
Masahiro Tsujimoto ⓘ https://orcid.org/0000-0002-9184-5556
Takeshi G. Tsuru ⓘ https://orcid.org/0000-0002-5504-4903
Ayşegül Tümer ⓘ https://orcid.org/0000-0002-3132-8776
Hiroyuki Uchida ⓘ https://orcid.org/0000-0003-1518-2188
Nagomi Uchida ⓘ https://orcid.org/0000-0002-5641-745X
Yuusuke Uchida ⓘ https://orcid.org/0000-0002-7962-4136
Hideki Uchiyama ⓘ https://orcid.org/0000-0003-4580-4021

Yoshihiro Ueda https://orcid.org/0000-0001-7821-6715
Jacco Vink https://orcid.org/0000-0002-4708-4219
Shin Watanabe https://orcid.org/0000-0003-0441-7404
Brian J. Williams https://orcid.org/0000-0003-2063-381X
Satoshi Yamada https://orcid.org/0000-0002-9754-3081
Shinya Yamada https://orcid.org/0000-0003-4808-893X
Hiroya Yamaguchi https://orcid.org/0000-0002-5092-6085
Kazutaka Yamaoka https://orcid.org/0000-0003-3841-0980
Noriko Yamasaki https://orcid.org/0000-0003-4885-5537
Makoto Yamauchi https://orcid.org/0000-0003-1100-1423
Tomokage Yoneyama https://orcid.org/0000-0002-2683-6856
Mihoko Yukita https://orcid.org/0000-0001-6366-3459
Irina Zhuravleva https://orcid.org/0000-0001-7630-8085
Amy Gall https://orcid.org/0000-0002-8260-2229
Sharon Mitrani https://orcid.org/0000-0001-6798-5447
Roi Rahin https://orcid.org/0000-0002-2842-0037

References

Arnaud, K. A. 1996, in ASP Conf. Ser. 101, Astronomical Data Analysis Software and Systems V, ed. G. H. Jacoby & J. Barnes (San Francisco, CA: ASP), 17
Bocchino, F., Miceli, M., & Troja, E. 2009, A&A, 498, 139
Brogan, C. L., & Troland, T. H. 2001, ApJ, 550, 799
Chiotellis, A., Zapartas, E., & Meyer, D. M. A. 2024, MNRAS, 531, 5109
Court, T., Badenes, C., Lee, S.-H., et al. 2024, ApJ, 962, 63
De Marco, O. 2009, PASP, 121, 316
Eckart, M. E., Brown, G. V., Chiao, M. P., et al. 2024, Proc. SPIE, 13093, 130931P
Fink, M., Kromer, M., Hillebrandt, W., et al. 2018, A&A, 618, A124
Foster, A. R. 2020, AN, 341, 191
Foster, A. R., Ji, L., Smith, R. K., & Brickhouse, N. S. 2012, ApJ, 756, 128
Fujimoto, R., Tanaka, Y., Inoue, H., et al. 1995, PASJ, 47, L31
González-Casanova, D. F., De Colle, F., Ramirez-Ruiz, E., & Lopez, L. A. 2014, ApJL, 781, L26
Grichener, A., & Soker, N. 2023, MNRAS, 523, 6041
Hayashi, T., Boissay-Malaquin, R., Tamura, K., et al. 2024, Proc. SPIE, 13093, 130931L
Hayato, A., Yamaguchi, H., Tamagawa, T., et al. 2010, ApJ, 725, 894
Holland-Ashford, T., Lopez, L. A., & Auchettl, K. 2020, ApJ, 903, 108
Hwang, U., Petre, R., & Hughes, J. P. 2000, ApJ, 532, 970
Ishisaki, Y., Kelley, R. L., Awaki, H., et al. 2022, Proc. SPIE, 12181, 121811S
Ishisaki, Y., Yamada, S., Seta, H., et al. 2018, JATIS, 4, 011217
Itoh, H., & Masai, K. 1989, MNRAS, 236, 885
Jones, D., & Boffin, H. M. J. 2017, NatAs, 1, 0117
Jordan, G. C., IV, Fisher, R. T., Townsley, D. M., et al. 2008, ApJ, 681, 1448
Kaastra, J. S., Mewe, R., & Nieuwenhuijzen, H. 1996, in UV and X-ray Spectroscopy of Astrophysical and Laboratory Plasmas, ed. K. Yamashita & T. Watanabe (Tokyo: Universal Academy Press), 411
Kaastra, J. S., Paerels, F. B. S., Durret, F., Schindler, S., & Richter, P. 2008, SSRv, 134, 155
Kaastra, J. S., Raassen, A. J. J., de Plaa, J., & Gu, L. 2024, SPEX X-ray spectral fitting package, v3.08.01, Zenodo, doi:10.5281/zenodo.12771915
Keohane, J. W., Reach, W. T., Rho, J., & Jarrett, T. H. 2007, ApJ, 654, 938
Kilbourne, C. A., Sawada, M., Tsujimoto, M., et al. 2018, PASJ, 70, 18
Lacey, C. K., Lazio, T. J. W., Kassim, N. E., et al. 2001, ApJ, 559, 954
Lodders, K., Palme, H., & Gail, H. P. 2009, LanB, 4B, 712
Lopez, L. A., Ramirez-Ruiz, E., Castro, D., & Pearson, S. 2013, ApJ, 764, 50
Maeda, K., & Nomoto, K. 2003, ApJ, 598, 1163
Meyer, D. M. A. 2021, MNRAS, 507, 4697
Mezger, P. G., Schraml, J., & Terzian, Y. 1967, ApJ, 150, 807
Miceli, M., Decourchelle, A., Ballet, J., et al. 2006, A&A, 453, 567
Miceli, M., Decourchelle, A., Ballet, J., et al. 2008, AdSpR, 41, 390
Mochizuki, Y., Tsujimoto, M., Kilbourne, C. A., et al. 2024, Proc. SPIE, 13093, 1309363
Moffett, D. A., & Reynolds, S. P. 1994, ApJ, 437, 705
Mori, K., Tomida, H., Nakajima, H., et al. 2022, Proc. SPIE, 12181, 121811T
Nagao, T., Maeda, K., Mattila, S., et al. 2024, A&A, 687, L17
Noda, H., Mori, K., Tomida, H., et al. 2025, PASJ, Advance Access
Ozawa, M., Koyama, K., Yamaguchi, H., Masai, K., & Tamagawa, T. 2009, ApJL, 706, L71
Plewa, T., Calder, A. C., & Lamb, D. Q. 2004, ApJL, 612, L37
Porter, F. S., Kilbourne, C. A., Chiao, M., et al. 2024, Proc. SPIE, 13093, 130931K
Pye, J. P., Becker, R. H., Seward, F. D., & Thomas, N. 1984, MNRAS, 207, 649
Reach, W. T., Rho, J., Tappe, A., et al. 2006, AJ, 131, 1479
Rho, J., & Petre, R. 1998, ApJL, 503, L167
Sano, H., Yoshiike, S., Yamane, Y., et al. 2021, ApJ, 919, 123
Sato, T., & Hughes, J. P. 2017, ApJ, 840, 112
Sato, T., Sawada, M., Maeda, K., Hughes, J. P., & Williams, B. J. 2025, ApJ, 986, 94
Sawada, M., Sato, T., Maeda, K., & Itonaga, K. 2025, PASJ, 77, 446
Shelton, R. L. 1999, ApJ, 521, 217
Shimizu, T., Masai, K., & Koyama, K. 2012, PASJ, 64, 24
Siegel, J., Dwarkadas, V. V., Frank, K. A., & Burrows, D. N. 2020, ApJ, 904, 175
Smith, R. K., Brickhouse, N. S., Liedahl, D. A., & Raymond, J. C. 2001, ApJL, 556, L91
Sun, L., & Chen, Y. 2020, ApJ, 893, 90
Tanaka, T., Yamaguchi, H., Wik, D. R., et al. 2018, ApJL, 866, L26
Tashiro, M. S. 2022, IJMPD, 31, 2230001
Townsley, D. M., Calder, A. C., Asida, S. M., et al. 2007, ApJ, 668, 1118
Ustamujic, S., Orlando, S., Miceli, M., et al. 2021, A&A, 654, A167
Westerhout, G. 1958, BAN, 14, 215
White, R. L., & Long, K. S. 1991, ApJ, 373, 543
Williams, B. J., Blair, W. P., Borkowski, K. J., et al. 2018, ApJL, 865, L13
Wynn-Williams, C. G. 1969, MNRAS, 142, 453
Yamaguchi, H., Acero, F., Li, C.-J., & Chu, Y.-H. 2021, ApJL, 910, L24
Yamaguchi, H., Badenes, C., Petre, R., et al. 2014, ApJL, 785, L27
Yamaguchi, H., Tanaka, T., Wik, D. R., et al. 2018, ApJL, 868, L35
Zhang, G.-Y., Slavin, J. D., Foster, A., et al. 2019, ApJ, 875, 81
Zhou, P., & Vink, J. 2018, A&A, 615, A150
Zhou, P., Zhang, G.-Y., Zhou, X., et al. 2022, ApJ, 931, 144
Zhou, X., Miceli, M., Bocchino, F., Orlando, S., & Chen, Y. 2011, MNRAS, 415, 244